WPJET1-PR(18) 20282

A V Chankin et al.

Assessment of the strength of kinetic effects of parallel electron transport in the SOL and divertor of JET high radiative H-mode plasmas using EDGE2D-EIRENE and KIPP codes

Preprint of Paper to be submitted for publication in
Plasma Physics and Controlled Fusion

This work has been carried out within the framework of the EUROfusion Consortium and has received funding from the Euratom research and training programme 2014-2018 under grant agreement No 633053. The views and opinions expressed herein do not necessarily reflect those of the European Commission.

Assessment of the strength of kinetic effects of parallel electron transport in the SOL and divertor of JET high radiative H-mode plasmas using EDGE2D-EIRENE and KIPP codes

A V Chankin[1], G Corrigan[2], A E Jaervinen[3], and JET Contributors*

EUROfusion Consortium, JET, Culham Science Centre, Abingdon, OX14 3DB, UK
[1]*Max-Planck-Institut für Plasmaphysik, Garching bei München, Boltzmannstr. 2, 85748, Germany*
[2]*CCFE, Culham Science Centre, Abingdon, OX13 3DB, UK*
[3]*Lawrence Livermore National Laboratory, Livermore, California 94550, USA*

Abstract

KInetic code for Plasma Periphery (KIPP) was used to assess the importance of kinetic effects of parallel electron transport in the SOL and divertor of JET high radiative H-mode inter-ELM plasma conditions with the ITER-like wall and strong nitrogen (N_2) injection. Plasma parameter profiles along magnetic field from one of the EDGE2D-EIRENE simulation cases were used as an input for KIPP runs. Profiles were maintained by particle and power sources. KIPP generated electron distribution functions, f_e, parallel power fluxes, electron-ion thermoforces, Debye sheath potential drops and electron sheath transmission factors at divertor targets. For heat fluxes in the main SOL, KIPP results showed deviations from classical (e.g. Braginskii) fluxes by factors typically ~ 1.5, sometimes up to 2, with the flux limiting for more upstream positions and flux enhancement near entrances to the divertor. In the divertor, at the same time, for radial positions closer to the separatrix, very large heat flux enhancement factors, up to 10 or even higher, indicative of a strong non-local heat transport, were found at the outer target, with f_e exhibiting bump-on-tail features at high energies. Under such extreme conditions, however, contributions of conductive power fluxes to total power fluxes were strongly reduced, with convective power fluxes becoming comparable, or sometimes exceeding, conductive power fluxes. Electron-ion thermoforce, on the other hand, which is known to be determined mostly by thermal and sub-thermal electrons, was found to be in a good agreement with Braginskii formulas, including the Z_{eff} dependence. Overall, KIPP results indicate, at least for plasma conditions used in this modelling, a sizable, but not dominant effect of kinetics on parallel electron transport.

* See the author list of "Litaudon et al, Nucl. Fusion **57** (2017) 102001

1. Introduction

Owing to their relatively low ion and electron temperatures, scrape-off layer (SOL) and divertor plasmas in tokamaks are usually considered as collisional, where collisional plasma transport equations, formulated e.g. in [1] can be applied. In one important respect, however, in application to parallel (along magnetic field lines) heat transport, plasma collisionality is often insufficient to justify the use of collisional (also often referred to as 'fluid') equations. It is well known that it is much less collisional high energy super-thermal electrons (with kinetic energies ~ $7T_e$, according to [2]), which are responsible for the bulk of the electron heat flux. In this paper expressions 'conductive power flux' and 'heat flux' will be used interchangeably.

Kinetic calculations typically reveal that at the 'hot' (high T_e) end of the flux tube ('upstream', using the nomenclature adopted in SOL and divertor studies) the heat flux is lower than predicted by the Braginskii formula ('heat flux limiting'), while at its 'cold' (low T_e) end ('downstream', near the entrance to the divertor, or inside of the divertor itself, including positions near divertor targets), the heat flux is higher than Braginskii ('heat flux enhancement'), see e.g. review paper [3] where results of several kinetic codes are assembled and compared with theoretical predictions. Kinetic effects are particularly strong during ELMs [4-6], with the electron heat transmission factor at the target plate, γ_e, increasing by an order of magnitude (up to 70) compared to its value 4.5 for strongly collisional plasmas [7]. According to [8], during an ELM the largest contribution to the increase in the total, ion plus electron, heat transmission factor at the divertor target $\gamma = \gamma_e + \gamma_i$ comes from ions (γ_i), while the increase in the inter-ELM periods is attributed mostly to electrons (γ_e), with γ_e rising by factor up to 50.

Due to the presence of high energy non-Maxwellian tails of the electron distribution function, f_e, near the target, kinetic rates of interaction between electrons and neutrals and impurities may increase by a large factor (see e.g. [9-12]). Such effects are however outside of the scope of the present paper, in which the emphasis is put on the ability of super-thermal electrons to create substantial deviations of the electron heat conduction from predictions based on the classical Braginskii formula, and their impact on heat transmission factors γ_e at the divertor target.

KInetic code for Plasma Periphery (KIPP) [13] is a kinetic code for parallel plasma transport in the SOL and divertor. The code is presently 1D2V, with one spatial coordinate (along magnetic field lines) and two velocity coordinates: parallel and gyro-averaged perpendicular velocities. The present version of the code modells kinetically only electrons, with the ion background assumed to be taken from elsewhere, e.g. from fluid codes. The code is based on the continuum discretisation finite volume scheme for the Vlasov-Fokker-Planck equation for parallel electron transport, using the operator splitting scheme to separate parallel propagation (free-streaming) and Coulomb collision operations. The code combines an implicit 2^{nd} order scheme for a full non-linear Coulomb collision operator with an explicit 2^{nd} order scheme for the free-streaming. Further details, as well as results of the code benchmarking, can be found in [14] and refs. therein. In the present work KIPP is used to assess the impact of kinetic effects of parallel electron transport on a number of transport coefficients, primarily parallel electron heat conduction coefficient and electron heat transmission factor at the divertor target. Parallel plasma profiles, taken from an EDGE2D-EIRENE (EDGE2D is the plasma part the code package, while EIRENE is the Monte-Carlo solver for neutrals [15-17]) solution simulating inter-ELM conditions for one of JET high radiation H-mode pulses, are maintained by power and particle sources in KIPP. Kinetic transport coefficients following from steady state KIPP solutions for a

number of radial positions in the SOL are compared with EDGE2D fluid coefficients. The particle source in KIPP is implemented by scaling the numerical factor before f_e to achieve the desire density, while the power source is introduced by the f_e's transformation based the expansion (or contraction) of the velocity grid by some factor (typically very small due to smallness of the time step) and an interpolation of distribution functions onto the original grid, with the subsequent density correction. For a Maxwellian f_e, this produces another Maxwellian with higher (or lower) T_e. Source terms in KIPP are therefore rather homogeneous, without favoring thermal or super-thermal electrons.

In this paper, in figures showing output from KIPP, profiles are plotted in internal dimensionless KIPP values, unless otherwise stated.

Section 2 is dedicated to heat carrying electrons (HCE), the notion widely used throughout the paper. They are responsible for the bulk of parallel electron heat flux. Their characteristic location in the velocity space, as well as their collision mean free paths, MFP, are established. The EDGE2D-EIRENE case and KIPP calculations based on its output are described in Section 3. Intrinsic limitations of KIPP, as well as those related to output profiles from the EDGE2D-EIRENE case, read by KIPP, are considered in section 4. Results of KIPP calculations are presented in section 5. Implementation of toroidal effects in KIPP, following from the curvilinear geometry of the magnetic equilibrium used to generate the EDGE2D grid, is discussed in sedction 6. Finally, conclusions from this work are drawn in section 7.

2. Heat carrying electrons (HCE)

The notion of heat carrying electrons (HCE) is critical for understanding kinetic effects of parallel electron heat transport. A number of factors point to high energy electrons as being primarily responsible for the heat flux. Parallel power flux scales with $v_{||} m_e v^2/2 \propto v^3$, where $v_{||}$ and v are parallel and total electron velocities. Lower collisionality of super-thermal electrons contributes to longer collision mean free paths (MFP) which scale as $v_{||}\tau_e \propto v_{||} v^{3/2} \propto v^{5/2}$, where τ_e - electron collision time. Finally, the number of high energy electrons includes the velocity phase space factor v^2 (for a given Δv). Altogether, the factor favouring high energy electrons is proportional to $v^{7.5}$. Against this acts the exponential decay of the number of high energy electrons $\exp(-m_e v^2/2T_e)$, following from the Maxwellian distribution. The compromise between these factors, according to kinetic calculations, leads to the energy of electrons, most capable of carrying heat, being of order 3-4 v_{th}, where $v_{th} = \sqrt{T_e/m_e}$ is electron thermal velocity.

Fig. 1 shows averaged power flux density $\langle f_e v_{||} v^2/2 \rangle$ (the averaging is done for a given absolute velocity v) vs. normalized total electron velocity v/v_{th} calculated in a KIPP case for a strongly collisional plasma with a small, 10%, T_e drop (data taken from [14]). The integral of this flux is also shown. This figure is similar to Fig. 7 of [2], slight differences in numbers can be attributed to a more precise collision operator in KIPP. Such a representation of the power flux density can be called a Chodura-type plot, in the name of the author of the frequently cited ref. [2] where such a figure was presented. The advantage of such a representation is in its inclusion

of the velocity space factor $4\pi v^2$ accounting for the velocity space between the spheres, which better reflects the contribution of high energy electrons. The maximum in $\langle f_e v_{||} v^2/2 \rangle$ in Fig. 1 is achieved at $v/v_{th} = 3.45$, corresponding to electron kinetic energy $m_e v^2/2 = 5.95\,T_e$. Negative numbers for lower velocities, $v/v_{th} < 2.53$ are attributed to the force of the parallel electric field $E_{||}$ caused by the electron-ion thermoforce: $-eE_{||} = 0.71\nabla T_e$ (the numerical coefficient is correct for plasmas with singly charged ions) [1]. This electric field force pulls electrons upstream, towards higher T_e. The critical electron energy for which this power flux becomes negative, $m_e v^2/2 = 3.2\,T_e$, is larger than the average kinetic electron energy $3/2\,T_e$, hence, all thermal electrons, and even electrons with energy twice the average kinetic energy, carry heat in the 'wrong' direction. The effect of the other part of $E_{||}$, caused by the parallel electron pressure gradient, is canceled by the effect of the pressure gradient itself.

An estimate for the collision MFP of HCE requires knowledge of their characteristic parallel and perpendicular velocities. Fig. 2 shows the 2D contour plot of the power flux density $f_e v_{||} v^2/2$ obtained in the same KIPP run as shown in Fig. 1. The maximum of this quantity is achieved at $v_{||}=2.74v_{th}$, $v_{\perp}=1.92v_{th}$, corresponding to a slightly lower kinetic energy, $5.60\,T_e$, than the $5.95\,T_e$ calculated for the maximum of $\langle f_e v_{||} v^2/2 \rangle$, the difference should be attributed to the contribution of the velocity space averaging factor $2\pi v_{\perp}$ in the latter. Using $5.95\,T_e$ as a characteristic HCE energy and fixing the $v_{||}/v_{\perp}$ ratio at 2.74/1.92=1.43, one obtains $v_{||}=2.82v_{th}$ and $v_{\perp}=1.98v_{th}$ as characteristic parallel and perpendicular HCE velocities. Very approximately, using the scaling v^3 for the collision time of super-thermal electrons, and taking into account the difference between the characteristic kinetic energy of HCE, $5.95\,T_e$, and the average electron energy $3/2T_e$, one obtains the factor $(5.95/1.5)^{3/2} = 7.90$ of increase in the collision time. Taking into account also higher parallel velocity of the HCE, $v_{||}=2.82v_{th}$, compared to the parallel velocity of a thermal electron with the parallel energy $T_e/2$: $v_{||th} = \sqrt{T_e/m_e} = v_{th}$, the overall factor of increase in the collision MFP of HCE, which scales as $\tau_{coll} v_{||}$, becomes $7.90 \times 2.82 = 22.3$.

The above estimate for the characteristic HCE kinetic energy and collision MFP is very approximate. If, for example, one used the kinetic energy $7.03T_e$, corresponding to the absolute electron velocity at which the integral of $\langle f_e v_{||} v^2/2 \rangle$ reaches half of its maximum, one would have obtained a factor 31.1 increase for the MFP of HCE.

Another issue with making more precise estimates for the MFP of HCE is related to the effect of electron-ion (e-i) and electron-electron (e-e) collisions. Most often, in the literature by electron collision time one assumes the e-i collision time given by (or coinciding with) Braginskii's electron collision time [1]:

$$\tau_e = \frac{3\sqrt{m_e}T_e^{3/2}}{4\sqrt{2\pi}\Lambda_c e^4 Z^2 n_i} \,. \qquad (1)$$

Here Λ_c is Coulomb logarithm, Z is ion charge, and the plasma neutrality, $Zn_i = n_e$, is assumed. When the plasma consists of more than one ion species, a substitution of $Z^2 n_i$ with $Z_{eff} n_e$ in numerical estimates is typically made. The collision time Eq. (1) coincides with 'electron collision time' used in [7].

Super-thermal electrons also collide with thermal electrons. According to [18], for electrons with $m_e \mathrm{v}^2/2 >> T_e$ parallel slowing down time $\tau_s^{e/e}$ due to their collisions with other electrons is ½ of that for e-i collisions, $\tau_s^{e/i}$, while their perpendicular diffusion time (in velocity space) τ_d, which describes pitch angle scattering, is the same for e-i and e-e collisions (Table 2 of [18]). In addition, e-e collisions, unlike e-i collisions, are very efficient in reducing energy of super-thermal electrons. The characteristic collision time of this process is $\tau_\varepsilon^{e/e} = m_e \mathrm{v}^2/8T_e \times \tau_s^{e/i}$ (Table 2 of [18]), which for $m_e \mathrm{v}^2/2 = 6T_e$ is equal to $1.5\tau_s^{e/i}$. Altogether, one can probably assume that the effect of e-e collisions reduces the overall collision time of super-thermal electrons, and hence, their collision MFP by factor 2 compared to the effect of only e-i collisions. Estimates in the previous paragraph gave for MFP of HCE the factor 22.3 – 31.1 increase compared to thermal electrons. Owing to the effect of e-e collisions, this factor should be reduced by about a half, giving only the factor 11.2 – 15.6 increase. Taking the average between these two numbers, we will be assuming that approximately the MFP of HCE can be characterized by factor 13 increase compared to the MFP of thermal electrons. The often used dimensionless collisionality, defined as $\nu^* = \nu_{coll} \mathrm{v}_{th}/L_\parallel$, where ν_{coll} is collision frequency calculated as $1/\tau_{coll}$ with the collision time calculated according to Eq. (1), should therefore be reduced by factor ≈ 13 when HCE are considered.

The above relation, $\nu^*_{HCE} \approx \nu^*_{th}/13$, gives a substantially smaller MFP increase for the HCE compared to thermal electrons than estimates based on the assumption that HCE energies are in the range of $3\mathrm{v}_{\mathrm{th}}$, with $\mathrm{v}_{\mathrm{th}} = \sqrt{T_e/m_e}$, and MFP scales as $(\mathrm{v}/\mathrm{v}_{\mathrm{th}})^4$ (see e.g. [19], where a factor 80 increase in the MFP of HCE is predicted). At the same time, a simple estimate made by using the characteristic HCE velocity $\mathrm{v} = 3.45\mathrm{v}_{\mathrm{th}}$, corresponding to the maximum power flux density in Fig. 1, together with the assumption that this factor obeys the scaling $\left(\mathrm{v}/\sqrt{3\mathrm{T_e}/m_e}\right)^4$ (for electron thermal energy $3/2\mathrm{T_e}$), gives the factor $(3.45/\sqrt{3})^4 = 15.7$ of the MFP increase, which is quite close to the factor 13 increase estimated above. The relatively close match between the two numbers arises from two deficiencies of the simple estimate which compensate one another: it doesn't account for higher parallel than perpendicular velocity of HCE and it ignores the effect of adding e-e to e-i collisions.

The impact of a fairly modest reduction in ν^* for HCE, only by factor ~13, could be seen in a series of self-similar KIPP runs with variable upstream collisionality, with different $\mathrm{T_e}$ drops from the stagnation point (upstream) to the divertor target [20]. In these cases deviations from Braginskii heat conduction coefficients were found to be only by factor ~1.5, both for the heat

flux limiting upstream and heat flux enhancement downstream. HCE appeared to be more collisional than could be expected from the simplest estimates based on the $(v/v_{th})^4$ scaling with $v_{HCE} = 3v_{th}$ and $v_{th} = \sqrt{T_e / m_e}$.

It has to be pointed out, however, that characteristic energies of electrons responsible for the bulk of the heat flux, as well as their collision MFP, are expected to be larger under conditions where extended non-Maxwellina tails for downstreaming electrons are found in kinetic calculations. This may the cases when T_e shows a very strong drop near the divertor target, such as e.g. in detached divertor conditions modelled by kinetic code ALLA [9]. Estimates made in this section therefore only give the lower boundary for HCE energies and their MFP.

3. EDGE2D-EIRENE case and KIPP runs

Radiative, partially detached operation in JET H-mode plasmas with the ITER-like wall was experimentally investigated and simulated with EDGE2D-EIRENE code package in divertor configurations [21]. The code cases, without drifts and currents, were ranged according to the divertor configuration (with the outer strike point on the vertical or horizontal target, with the inner strike point being on the vertical target in both configurations), input power into the discharge and nitrogen radiation levels. One of the catalogued EDGE2D-EIRENE cases ('ajarvin/edge2d/jet/85274/feb2116/seq/#3', not listed in the tables in [21]) was chosen to provide the plasma background for KIPP simulations. This case corresponds to the JET discharge with both strike points on vertical targets, 8 MW of input power and 5 MW of nitrogen radiation in a the mostly deuterium plasma. Deuterium radiation, together with a small amount of the radiation on beryllium impurities, was below 0.5 MW. Tungsten radiation at the plasma edge was negligible, for this reason tungsten was not included as an ion species, which consisted of deuterium (D), beryllium (Be) and nitrogen (N) in the simulations. The nitrogen injection levels in EDGE2D-EIRNE cases modelled in [21] are not quoted. This is because nitrogen was assumed as a recycling impurity in the modelling (EDGE2D-EIRENE has only two possibilities: fully recycling or fully absorbing impurity), whereas in reality it is a partly recycling impurity. The N content in the plasma was maintained by 'extra neutral flux' feedbacked on the impurity radiation level (5 MW, as stated above). The amount of this 'extra' flux was 1.5×10^{20}, in electrons per second. Similar to the main (deuterium) neutrals, nitrogen neutrals (N_2) were pumped at the pump surfaces specified in EDGE2D at the rate equal to the 'extra' flux, which in indicates the steady state conditions reached in the modelling case.

For the given discharge parameters, the EDGE2D-EIRENE solution yielded large variations of electron temperature, T_e, along field lines in the SOL/divertor plasma, ranging from 90 eV in the main SOL to below 1eV at target plates. Under these conditions strong contributions of kinetic effects to the parallel electron transport could be expected.

The EDGE2D grid used in the simulation is shown in Fig. 3, and the expanded view of the grid in the divertor region is shown in Fig. 4. Also shown in this figure are numbered cells of radial positions indicating poloidal 'rings' chosen for KIPP runs, which will be referred to below as 'slices' with numbers i from 1 to 6. Slice i = 1 belongs to the first poloidal ring just outside of the magnetic separatrix. Radial profiles of n_e, T_e and T_i at the outer midplane (OMP) position from the EDGE2D-EIRENE output are shown in Fig. 5, and target profiles of T_e, n_e and ion saturation current density across target surfaces j_{sat} are shown in Fig. 6. Small T_e around strike point

positions and j_{sat} having its maxima outside of these positions indicate partial detachment near strike points.

EDGE2D allows extraction of plasma parameters along parallel direction (along magnetic field lines). The most important parameters extracted at cell centres are electron and ion temperatures and Z_{eff}. Average ion parallel velocities were extracted at cell faces. In addition, for comparison with the KIPP output, parallel electron convective and conductive power fluxes were also extracted at cell faces. During KIPP runs, EDGE2D parameters (input for KIPP) were maintained by particle and power sources. The most important macroscopic output parameters from KIPP are electron parallel conductive power flux (through cell faces) and ion-electron thermoforce (at cell centres) alongside electron distribution functions, f_e, at cell centres.

KIPP calculations described in the present paper can't be considered as fully self-consistent kinetic calculations, rather, they allow one to assess the potential strength of kinetic effects under different plasma conditions. The strategy of KIPP development, from the beginning of its creation, was to add kinetic effects to most efficient present day 2D edge fluid codes such as EDGE2D and SOLPS [22,23]. These codes use realistic magnetic configurations, include details of the divertor structure and sophisticated treatment of neutrals transport and atomic rates of excitation, ionization etc., carried out by the Monte Carlo solver EIRENE coupled to EDGE2D and SOLPS. Absence of kinetic effects related to charged particles is however one of the weak points of these codes. Efforts to couple KIPP with SOLPS are presently underway at IPP/Garching. Such a coupling is considered as a way of increasing predictive capability of edge fluid codes by adding new physics without losing their strong points. It could also minimize the run time of the coupled kinetic-fluid code. At present, even convergence of 2D fluid code calculations for some cases can take weeks, and the full replacement of the fluid plasma treatment with the kinetic one would dramatically increase the CPU consumption.

KIPP employs a 2nd order scheme for parallel propagation of electrons, which relies on linear interpolations between cell centre and cell face values. For this reason sharp changes in plasma parameters from cell to cell reduce the code accuracy. It was found already in the first runs that smoothness of KIPP output profiles could be increased if the grid shown in Fig. 3, with 88 cells in the poloidal direction, was made finer. As a result, the number of grid cells in the poloidal direction was increased by factor 2, from 88 to 176, by dividing each cell if half and interpolating EDGE2D output profiles from original to new, thinner cells. This led to elimination of some artifacts in KIPP output profiles caused by strongly non-linear features in the input data (output from EDGE2D). Other limitations of KIPP influencing its ability to provide correct output will be discussed in the next section.

Since the EDGE2D-EIRENE case had no parallel currents, ambipolarity of parallel plasma fluxes was assumed. In KIPP this is achieved via adjustments of parallel electric field ($E_{||}$) inside of cells, resulting in equal electron and ion fluxes through cell faces (with ion fluxes being an input from EDGE2D). Ambipolarity at boundary cell faces, adjacent to targets, was achieved by calculations of Debye potential sheath drops which made electron fluxes equal to ion fluxes.

In the EDGE2D-EIRENE case, heat flux limits were used for both ions and electrons, with heat conduction coefficients given by $\kappa_{||}/(1+|q_{||}/q_{fl}|)$, $q_{||} = -\kappa_{||}\nabla_{||}T$, with coefficients $\kappa_{||}$

calculated according to the '21 moment approach'. The electron coefficient $\kappa_{e\|}$ was found to be very close to the Braginkii result. Heat fluxes are limited by $q_{fl} = \alpha n T^{3/2} / \sqrt{m}$, with coefficients α set to 10 for both ions and electrons for the case analysed. Coefficients equal to 10 imply a very weak limitation of the theoretical heat flux coefficient applicable to strongly collisional plasmas.

In order to cover the wide range of electron temperature, a logarithmic velocity grid was used, with 400×200 grid cells (400 for parallel velocity to cover both positive and negative values, and 200 for perpendicular velocity) and an increase in the cell size by factor 1.02 from each cell towards the adjacent cell, at higher absolute velocity, for both parallel and perpendicular velocities. The cell linear size was thus varied by factor ≈ 52, translated into factor ≈ 2700 for electron energies.

KIPP uses dimensionless parameters. Electron velocities, in particular, are normalized to $\sqrt{T_o / m_e}$, with T_o being the highest T_e along a given field line, for each radial position. The maximum parallel and perpendicular velocities of the velocity grid are $7\sqrt{T_o / m_e}$.

Power and particle sources and sinks, aimed at maintaining given (extracted from the EDGE2D-EIRENE solution) parallel profiles, were, as explained in Sec. 1, rather homogeneous across the velocity space, instead of e.g. targeting super-thermal tails for power sinks, for the case of local T_e being << ionization potential of neutral atoms. Implementation of kinetic excitation, ionization and other rates in KIPP will be done later. In this study, the emphasis is put on the effects of electron parallel transport and Coulomb collisions.

4. Limitations of KIPP

As was already pointed out in the previous section, KIPP runs are subject to a number of limitations. One of them is related to smoothness of parallel profiles of plasma parameters. For this reason, the number of spatial cells in the present study was doubled (see above). In particular, inaccuracies in the linear interpolation of cell centre T_e values on cell faces led to inaccuracies in the calculation of electron conductive power flux, $q_{e,cond}$, which is defined as the total electron power flux q_e minus convective electron heat flux $q_{e,conv} = 5/2 \Gamma T_e$, and which is to be compared with EDGE2D-EIRENE and Braginskii conductive power fluxes. Such inaccuracies increase when T_e profiles become strongly non-linear (or, more generally, when the 2nd derivative becomes large). There are also inaccuracies in the calculation of electron particle fluxes through cell faces. In KIPP, electron cell face fluxes have to match ion cell face fluxes taken from EDGE2D. The match, as was pointed out earlier, is achieved by the $E_\|$ adjustment, which has to maintain the parallel electron momentum, such that parallel ion velocities in cell centres could be matched. In the presence of strongly non-linear profiles this match cannot be achieved and corrective cell face fluxes have to be used. The ratio of corrective to original fluxes has to be small for the results to be trustable. This ratio is one of the KIPP output paramters after the completion of each time step. Finally, there is some contribution from the Monte Carlo noise, mostly affecting electron density profiles.

Strongly non-rectangular cells, in particular, EDGE2D grid cells around the X-point, present

another numerical problem for KIPP whose equations employ the philosophy of a flux tube. When reading EDGE2D-EIRENE output data into KIPP, it is implicitly assumed that an infinitely narrow flux tube passes through centres of EDGE2D cells. In reality, EDGE2D solves equations in flux coordinates, so their reconstruction in the Cartesian coordinate system leads to inaccuracies in the mapping, resulting in wiggles in the profiles. The mapping inaccuracy depends on local change of grid size which is the largest near the X-point. In the future, correcting coefficients for transferring EDGE2D output data to KIPP will be applied, which will generate correct temperature derivatives that must be used in KIPP in order to match EDGE2D and KIPP fluxes.

Effects of toroidal geometry, on the other hand, are presently incorporated in the default version of KIPP. They can be switched on and off. Code results with and without toroidal effects were found to be almost indistinguishable, see the discussion in Sec. 6.

One of the strongest limitations of kinetic codes is smallness of the time step which, ideally, has to be much smaller than electron collision times of electrons with both electrons and ions in the most collisional spatial cell, which typically is one of the two boundary cells near the targets. By default, in KIPP the time step used is ≈ 2.5% of Braginskii electron-ion collision time ([1], Eq.(2.5e)) in the most collisional cell. This time step can however be increased by factor ~10 initially in order to reach the steady state for upstream, less collisional plasma, faster. It typically takes about one week of calculations on the Hydra machine at IPP/Garching, using 256 processors, to reach the steady state for conditions when T_e falls by factor ~ 100 from upstream to the target(s).

5. KIPP results

In this section results of KIPP calculations along field lines from the inner (IT) to the outer target (OT) for 6 radial positions ('slices') indicated in Fig. 4 and numbered from 1 to 6 are presented. The positions will be indicated by index 'i' in the rest of the paper. In all these cases dimensionless upstream electron collisionalities ν^*, defined as the ratio of the half of the parallel length from one target to the other, to the electron-ion (e-i) collision mean free path (MFP) for parameters of the 'hottest' (highest T_e) cell, calculated according to Braginskii's formula Eq.(2.5e) for Z_i=1, were quite similar, varying only between 14.2 and 19.3. Z_{eff} in 'hottest' cells were close to unity for all slices. The division by 2 is required for the direct comparison with formulas in [7], where the parallel length is taken to be the distance between the upstream position and the target. According to [7] (Eq.(4.127), $\nu^* > 15$ gives the condition for a significant T_e drop along the field line. Hence, EDGE2D-EIRENE results analysed here are expected to have only moderate T_e variations along field lines, which is indeed the case for T_e variations in the main SOL plasma, outside of the divertor. For slices i = 1 to 4, closer to the separatrix, an additional strong T_e drop from the entrance to the divertor down to divertor targets follows from the EDGE2D-EIRENE simulation, which is attributed to strong radiation in the divertor, mostly on nitrogen ions. In this paper, EDGE2D-EIRENE and KIPP results will be presented only for slices i = 1, 3 and 6, since they represent qualitatively different plasma parameter variations along field lines. Results for the remaining slices, i = 2, 4 and 5 are transitional, between the selected slices.

For parallel electron heat fluxes (or 'conductive power fluxes') three different quantities will be plotted in the figures: q_{KIPP} from KIPP calculations, q_{EDGE2D} from the EDGE2D-EIRENE output, and q_{Brag}, calculated from the Braginskii formula (1st term on the right hand side of Eq. (2.11) of [1]) for given parallel T_e and Z_{eff} profiles (dependence on Z_{eff} is discussed below). These conductive power fluxes will be compared with each other. Strong deviations of q_{KIPP} from q_{EDGE2D} and q_{Brag} (the two latter fluxes were found to e close to each other) indicate the importance of kinetic effects in the parallel electron transport. In addition, parallel profiles of convective power fluxes q_{conv}, calculated as $5/2\Gamma T_e$, where Γ is parallel plasma (ambipolar) particle flux and T_e – electron temperature at a cell face, will also be presented. Values of these particle fluxes coincide with the direct output from the EDGE2D-EIRENE case.

Conductive power fluxes q_{theory} for arbitrary Z_{eff} are taken from the Appendix of [24]:

$$q_{e\|,cond} = -\frac{13.58}{Z_{eff}} \frac{Z_{eff} + 0.21}{Z_{eff} + 4.2} \frac{n_e T_e \tau_e}{m_e} \nabla_{\|} T_e . \qquad (2)$$

For $Z_{eff} = 1$ the ratio $\frac{13.58}{Z_{eff}} \frac{Z_{eff} + 0.21}{Z_{eff} + 4.2}$ gives Braginskii's coefficient 3.16.

For ion-electron thermoforce, Braginskii's coefficient 0.71 in the expression $R_T = -0.71 n_e \nabla_{\|} T_e$ for the friction force acting on electrons with ion charge Z_i=1 was replaced with $1.5 \times \frac{Z_{eff} + 0.55}{Z_{eff} + 2.273}$. This coefficient matches Braginskii's coefficients for Z_i = 1 and ∞, and deviates from these coefficients for Z_i = 2, 3 and 4 by less than 1.1%.

Most detailed analysis of kinetic effects will be done for the slice i=3, for which relatively smooth parallel profiles of plasma parameters, primarily of T_e, follow from the EDGE2D-EIRENE solution. At the same time, this slice reveals most important features of both local and non-local effects of parallel electron transport. Results for this slice will be presented in Section 5.1. For the slice i=1 with the highest upstream T_e, extra complications arise due to very large T_e drops near the X-point. Analysis of KIPP results for this slice will be less detailed than for the slice i=3. Results for this slice will be presented in Section 5.2. Profiles of both EDGE2D-EIRNE and KIPP results for the slice i=2 are qualitatively similar to those of slice i=1, so they will not be presented here. Finally, profiles for the slice i=6 with the lowest upstream T_e will be presented in Section 5.3. Profile features for slices i=4 and 5 are transitional between slices i=3 and 6, they will not be presented here.

5.1 KIPP results for slice i = 3

Parallel profiles of the three conductive electron power fluxes: q_{KIPP}, q_{EDGE2D} and q_{Brag}, as well as the profile of the convective electron power flux q_{conv} and electron temperature T_e, are plotted in Fig. 7. Positive power fluxes are directed from the inner to outer target. As was pointed out in Sec. 3, the number of cells used to plot profiles in Fig. 7 was doubled, compared to the

number of cells in the EDGE2D-EIRENE case, to improve smoothness of input profiles for KIPP calculations. The maximum upstream T_e is 52.2 eV, and target T_e were 0.93 and 1.18 eV for inner and outer targets, respectively. Dimensionless upstream (thermal) electron collisionality defined in Sec. 2, for the cell with the highest T_e is $\nu^* = 17.5$.

There is a reasonable agreement between q_{EDGE2D} and q_{Brag} in the main SOL, accept for the region near the entrance to the outer divertor. The disagreement may be attributed to a number of factors, e.g. to the influence of the heat flux limiting adopted in EDGE2D-EIRENE or to the deviation of the heat flux calculated according to the 21 moment approach in EDGE2D from the Braginskii heat flux even for the case without the flux limit. One can clearly see the effect of non-rectangular cells in the wiggles of q_{Brag} near entrances to the divertor, as well as an unexpected increase in the q_{Brag} derivative at $s_{||} > 77$ m ($s_{||}$ is the distance from the inner target along field lines). The moderate heat flux limiting in the main SOL can be seen, with q_{KIPP} being less than q_{Brag} and q_{EDGE2D} by factor < 1.5. The convective power flux q_{conv} is mostly negative, reflecting plasma flow from the outer to inner target, except for the outer divertor region where it is positive due to the plasma sink at the divertor target. The cause of the parallel plasma flow in the main SOL is not analysed in the present paper.

Fig. 8 shows various output parameters from the EDGE2D-EIRENE case. Large, factor ~ 2 difference between upstream T_e and T_i in favour of the latter is consistent with the upstream collisionality $\nu^* = 17.5$, far below the $\nu^* = 50$ value necessary for thermal equilibration between electrons and ions, $T_e \approx T_i$, (Eq. (4.137) of [7]). Upstream parameters indicate that the plasma is moderately collisional. The $n_e(T_e + T_i + m_i V_{i||}^2)$ profile plotted in Fig.8 corresponds to parallel stress for the case of the Cartesian geometry, the quantity which tends to be conserved along field lines in the absence of parallel momentum sources. The drop of this parameter by a factor 2 to 3 towards the targets is close to the expected factor 2 drop due to the plasma acceleration up the ion sound speed, implying that the momentum loss at this slice is insignificant, and that the plasma is well attached to the targets.

Figs. 9a,b are the zoomed versions of Fig. 7, showing profiles in the inner and outer divertor. In the outer divertor (Fig. 9b), profiles of q_{EDGE2D} and q_{Brag} almost match, but q_{KIPP} is much higher, by factor 10 near the OT, indicating strong non-locality of the conductive power flux. In the inner divertor, an unexpected rise of q_{Brag} for $s_{||} > 5$ m should be attributed to wiggles caused by non-rectangular cells discussed earlier. Near the IT (Fig. 9a) q_{KIPP} is much higher than q_{EDGE2D} and q_{Brag}. The KIPP power flux q_{KIPP} shows oscillations which can be caused by an inaccuracy of its calculation owing to the relatively large convective power flux q_{conv} which has to be subtracted from the total electron power flux to obtain q_{KIPP}, and an imprecision of the T_e interpolation from cell centres to cell faces, as discussed in Sec. 4. The averaged value of q_{KIPP} near IT is much greater than q_{EDGE2D}.

Relative contributions of local and non-local mechanisms to the conductive power flux can be assessed from Chodura-type plots shown in Figs. 10a,b. In such plots throughout the paper the thermal velocity v_{th} is calculated for the highest T_e upstream, which is used for normalization of velocities in KIPP calculations. The total conductive power flux can be calculated by simply integrating the power flux over the value of the X-axis, as is the case of Fig. 1. From Fig. 10b one can see that the non-local contribution to the conductive power flux density at OT, coming from the bump-on-tail feature, is dominant. Non-local electrons responsible for the bulk of the heat flux have energies close to HCE energies of upstream upstream electrons with $v = 3 - 4v_{th}$, hence, they are likely to originate from the region with the highest T_e upstream. At the IT (Fig. 10a) the contribution of the bump-on-tail feature is less pronounced.

It is important to note that, despite q_{KIPP} in Figs. 9a,b are much higher than q_{EDGE2D} and q_{Brag} closer to divertor targets, the increase in conductive electron power fluxs q_{KIPP} doesn't strongly affect total electron power fluxes to targets due to large contributions of convective electron power fluxes q_{conv} which are of the same order as q_{KIPP}.

The impact of non-locality on the power flux is somewhat stronger at OT than IT, as follows from larger q_{KIPP} / q_{EDGE2D} ratio for average power fluxes near OT and a more significant bump-on-tail feature of the conductive power flux density distribution. This is likely to be related to the higher plasma collisionality in the inner divertor, leading to stronger attenuation of high energy electrons coming from upstream by more frequent Coulomb collisions. Fig. 11 shows the log10 plot of dimensionless collisionality ν^*_{HCE}, calculated as electron dimensionless collisionality ν^* divided by 13, to reflect the expected collisionality of HCE in the high collisionality limit, see Sec. 2. Unlike the global upstream electron collisionality $\nu^* = \nu_{coll} v_{th} / L_{||}$, ν^* in Fig. 11 is calculated differently, using the local collisionality $\nu_{coll} v_{th} / \lambda_{T_e}$, where $\lambda_{T_e} = \left| T_e / \nabla_{||} T_e \right|$ is the parallel decay length of electron temperature. As one can see, both in the divertor and in the SOL, at ~ 10 m away from the entrance to the divertor, ν^* is larger in, and close to, the inner divertor. The large rise in this quantity upstream, towards the stagnation point at $s_{||} \approx 56$ m, is attributed to very small T_e gradients. In this region the ratio $\lambda_{T_e} / \lambda_{HCE}$ as a figure of merit for local electron collisionality loses its sense, and collisionality can only be defined globally, as $\nu^* = \nu_{coll} v_{th} / L_{||}$ due to the strong non-local electron transport. At the entrance to the outer divertor and in the main SOL, within ≈ 13 m from the divertor entrance, ν^* falls below unity, indicating that HCE are moderately collisional, which results in not very strong deviation of conductive power fluxes from Braginskii fluxes, by factor < 1.5, as was shown above (Fig. 7).

In contrast to conductive power fluxes near the targets, Chodura-type conductive power flux density profiles, shown in Figs. 12a,b for positions of entrances to the divertor indicated by vertical dashed lines in Fig. 7, look similar to the profiles shown in Fig. 1. They don't indicate contributions of high energy tails above HCE energies for strongly collisional cases.

In addition to conductive power fluxes, electron kinetic effects are also expected to influence electron-ion (e-i) thermoforce $R_T = -k_T n_e \nabla_{||} T_e$, where $k_T = 1.5(Z_{eff} + 0.55)/(Z_{eff} + 2.273)$ (see Sec. 5). The e-i thermoforce and the compensating electric field $E_T = k_T \nabla_{||} T_e / e$ are calculated at each time step during the KIPP run. Parallel profiles of E_T, following from the KIPP calculations and from the theoretical formula using the k_T coefficient above, expressed in internal dimensionless KIPP units, are plotted in the top box of Fig. 13. A very good match between the two quantities can be seen in the figure for all cells. The bottom box shows thermoforce coefficients k_T calculated using KIPP and the above formula for $k_T(Z_{eff})$, together with the Z_{eff} profile. The horizontal dash-dotted line corresponds to $k_T = 0.71$, the theoretical coefficient for $Z_{eff} = 1$. Coefficients extracted from KIPP results require division by $\nabla_{||} T_e$, leading to singularities near the T_e maximum. In accordance with a good agreement between KIPP and theoretical values for E_T, a good agreement between the two k_T coefficients can also be seen (except for the singularity feature). Z_{eff} (which is an output from EDGE2D-EIRENE) is close to unity near the targets due to the ion-impurity thermoforce which moves impurity ions upstream. The good agreement between the two E_T profiles, as well as the two k_T profiles, could be expected, since the e-i thermoforce is known to be caused by the friction force exerted on ions mostly by thermal and sub-thermal electrons which are little affected by non-local transport of high energy electrons.

Finally, Debye sheath potential drops and electron power fluxes through the sheath can also be affected by electron kinetic effects. The Debye sheath potential drop coefficients $e\Delta\Phi/T_e$ at the targets, where $\Delta\Phi$ is the Debye sheath drop and T_e is target temperature, are 2.84 and 2.83 for IT and OT, respectively, which agrees well with Eq. (2.60) of [7] for target T_i/T_e ratios following from EDGE2D-EIRENE (close to 1 for i = 3). This shows that, at least in this case, super-thermal bump-on-tail electrons contribute very little to the formation of sheath potential drops. At the same time, electron heat transmission factors $\gamma_e = q_{e,tar}/(\Gamma_{e,tar} T_{e,tar})$, where $q_{e,tar}$ is the total electron power flux through boundary cell faces, $\Gamma_{e,tar}$ is electron particle flux through the sheath, and $T_{e,tar}$ is electron temperature at the sheath (which coincides with the boundary cell face), are 5.49 and 7.10 for IT and OT, respectively. This should be compared with values of 4.8 for both targets following from Eq. (2.90) of [7] which doesn't include the contribution from the plasma pre-sheath. Higher γ_e from KIPP than from [7] can be explained by the contribution of super-thermal electrons to the conductive power flux, especially at OT, whereas at IT the power flux is dominated by convection.

5.2 KIPP results for slice i = 1

Parallel profiles of the three conductive electron power fluxes, the convective electron power flux and T_e are shown in Fig. 14. Notations are the same as in Fig. 7 for the slice i = 3. The maximum upstream T_e is 90.4 eV, and target T_e are 0.26 and 0.75 eV, for inner and outer targets, respectively. Dimensionless upstream electron collisionality defined similarly to the case with i = 3 is $\nu_e^* = 14.2$.

Similar to the case with i = 3, a good agreement between q_{EDGE2D} and q_{Brag} in the main SOL, away from the divertor, can be seen, with q_{KIPP} being smaller than these two fluxes by factor up to ~ 1.5 in the most of the main SOL, indicating heat flux limiting due to kinetic effects. Large spikes in q_{KIPP} at positions of maximum T_e gradients, on the other hand, indicate large heat flux enhancement. The contribution of the convective power flux q_{conv} to the total power flux is much lower for this slice compared to the i =3 slice. Very large T_e drops near and at entrances to divertors do not only reduce the reliability of KIPP results, as discussed in Sec. 4, but also put into question correctness of EDGE2D-EIRENE results. In future tests, similar to the ones described in this paper, or in coupled EDGE2D-KIPP runs, the resolution of the EDGE2D grid may need to be increased in order to avoid very large T_e drops between cells close to the X-point.

Fig. 15 shows various output parameters from the EDGE2D-EIRENE case, as in Fig. 8 for the slice i = 3. Large drops in $n_e(T_e + T_i + m_i V_{i\|}^2)$ towards targets indicate conditions of a partial detachment.

Figs. 16a,b are zoomed versions of Fig. 14, showing the same profiles, but only in the inner and outer divertors, respectively. q_{EDGE2D} and q_{Brag} are almost negligible in both divertors, being much less than q_{KIPP}, whereas convective power fluxes q_{conv} are larger than conductive power fluxes q_{KIPP}. This, similarly to the situation with the slice i = 3, indicates that even greatly increased kinetic conductive power fluxes q_{KIPP} don't strongly raise total electron power fluxes to divertor targets which are dominated by large convective power fluxes q_{conv}.

Figs. 19a,b show Chodura-type plots of conductive power flux densities vs. dimensionless absolute velocity, similar to Figs. 10a,b for the slice i = 3, in the cells adjacent to outer and inner divertor targets, respectively. The bump-on-tail features of these profiles are weaker than for the slice i = 3, especially at IT, apparently due to very strong attenuation of HCE from upstream on their way to the targets by Coulomb collisions: despite peak densities, at the targets, are lower for the i = 1 slice, compared to i =3, average divertor densities are higher.

At the entrances to divertors, Chodura-type plots, shown in Figs. 20a,b, in difference to the i =3 slice, indicate the strong presence of non-local electrons coming from the hottest (with the highest T_e) positions along the field line. In Fig. 20b for the entrance at the outer divertor, their presence manifests itself as weakly attenuated bump-on-tail feature, while in Fig. 20a for the entrance at the inner divertor, the contribution from strongly non-local electrons can be clearly seen.

Profiles of electric field caused by the e-i thermoforce, together with coefficients k_T are shown in Fig. 19. They are calculated in the same way as profiles shown in Fig. 13 for the i = 3 slice. As in that slice, a good match between KIPP and theoretical quantities can be seen, except for values close to divertors which are apparently strongly influenced by super-thermal strongly non-local electrons. This explanation agrees with Chodura-type plots in Figs. 18a,b which indicate the strong presence of such electrons, unlike for the i = 3 slice, where such a presence can't be seen (Figs. 12a,b).

The Debye sheath potential drop coefficients at the targets are 2.58 and 2.66 for IT and OT, respectively, which is somewhat lower than according to Eq. (2.60) of [7] for target T_i/T_e ratios close to 1, which follow from EDGE2D-EIRENE. Electron heat transmission factors γ_e are 5.17 and 5.28 for IT and OT, respectively. Values close to the theoretical value of 4.8 for strongly collisional plasmas, following from Eq. (2.90) of [7], are not surprising, since electron power flux to the targets is dominated by convection.

5.3 KIPP results for slice i = 6

Parallel profiles of conductive and convective electron electron power fluxes, together with the T_e profile, are shown in Fig. 22. Notations are the same as in Fig. 7. The T_e profile shows a rather moderate drop to the targets. Heat flux limiting in the regions of sharp T_e drops is relatively small. Overall, the power fluxes exhibit the same features as for other slices. The contribution of power convection is larger than for other slices. The maximum upstream T_e is 31.1 eV, and target T_e are 8.26 and 23.48 eV, for inner and outer targets, respectively. Dimensionless upstream electron collisionality defined similarly to the case with i = 3 is $\nu^* = 19.0$.

Fig. 21 shows the same output parameters from the EDGE2D-EIRENE case as shown in Figs. 8 and 15. Flatness of the $n_e(T_e + T_i + m_i V_{i\|}^2)$ profile and a relatively small n_e variation along the field line indicate that the plasma is in a moderate recycling regime with a small momentum loss in the divertor.

Figs. 22a,b are zoomed versions of Fig. 20, showing the same profiles, but only in the inner and outer divertors, respectively. Due to low recycling in this slice, q_{EDGE2D} and q_{Brag} are not too much different from q_{KIPP}. The electron conductive power flux q_{KIPP} is larger than the conductive power flux q_{conv}, which is a consequence of low recycling at the targets.

Chodura-type plots are shown in Figs. 23a,b for IT and OT, respectively. Both have no bump-on-tail features and look rather similar to that in [2] (Fig. 1) for the case of strongly collisional plasmas. The profile at IT shows a somewhat extended tail for higher electron energies, probably due to the stronger T_e drop at IT than at OT.

Electron distribution functions and conductive power flux densities for positions at the entrances to the divertor look similar to those shown for the i =3 slice and therefore are not presented here.

Overall, these results, as well as results from slices i = 2, 4 and 5, not presented here (their results are intermediate, between slices i = 1, 3 and 6), reveal that the heat flux limiting for the analysed EDGE2D-EIRENE case typically doesn't exceed factors ~ 1.5. Flux enhancement factors downstream, on the other hand, may be large, of order 10 or even larger. When this is the case, however, electron heat convection becomes comparable to conduction, or even larger than it, so the impact of electron kinetic effects on the total electron power flux to the target isn't particularly strong. It has to be pointed out, however, that kinetic effects related only to the parallel electron propagation (free-streaming) and Coulomb collisions were included in the KIPP modelling presented in this paper. Higher kinetic rates of electrons interaction with neutrals and impurities, caused by non-Maxwellian tails of super-thermal electrons, might result in such

changes of parallel profiles of macroscopic plasma parameters that kinetic effects may become more important.

Fig. 24 shows profiles of the electric field E_T caused by the e-i thermoforce, thermoforce coefficients and Z_{eff}. Notations are the same as in Fig. 13. In the main SOL, outside of the divertor, the two E_T profiles, calculated by KIPP and by using the theoretical value for collisional plasmas, show a very good match, similar to the situation for the slice i = 3, as well as for slices 4 and 5, not presented here. In difference to the slice i = 3, however, the two profiles deviate from each other in the divertor, especially near the targets. This can be attributed to the the Debye sheath cut-off effect on f_e, since, unlike in the boundary cells for slices i = 1 and 3, which are strongly collisional, this cells for the slice i = 6 are weakly collisional. This effect is stronger at the OT, indicated by a larger difference in the thermoforce coefficients seen in the bottom figure. By the cell collisionality here one understands the ratio of the parallel cell size to the collision MFP, which is 3.5×10^{-3} at OT, compared to e.g. 85 for the boundary cell at OT in slice i = 3. In Fig. 25 averaged over perpendicular velocity electron distribution functions f_e at boundary cells adjacent to OT for slices i = 6 and 3 are shown. Axes values are not related to each other, since velocities were normalized using highest upstream T_e for each slice separately. For i = 6, the Debye sheath cut-off effect can be seen at $v_{||}/v_{\perp} \approx -2$, unlike for i =3, were Coulomb collisions resulted in smoothing of it's effect.

Debye potential drops at the targets are 2.81 and 2.93 for IT and OT, respectively, which are slightly higher than the numbers 2.70 and 2.83 following from Eq. (2.60) of [7], indicating a possible (minor) role of super-thermal electrons in the formation of the Debye sheath. Electron heat transmission factors are 6.25 and 5.60 for IT and OT, respectively.

6. Implementation of toroidal effects in KIPP

The physical origin of the influence of toroidal effects on the plasma in a strong magnetic field is explained in [25]. It was used for implementation of toroidal effect in KIPP. Only effects related to the parallel electron propagation were implemented in KIPP. Cross-field drifts were not considered.

According to [25], implementation of toroidal effects into 1D (along magnetic field B) conservation equations can be done by introducing variable cross-section of the flux tube and the effect of the mirror force acting on a charged particle. In KIPP, by default cell faces have different cross-sections, proportional to major radius R, which ensures constant magnetic field flux through cell faces, since $B \propto 1/R$ for low beta edge plasmas. Mirror force $-\mu\nabla B \cdot \frac{\mathbf{B}}{B} = \frac{mv_{\perp}^2}{2R}\frac{\partial R}{\partial s_{||}}$ also affects perpendicular velocity owing to $\frac{dv_{\perp}^2}{dt} = -\frac{dv_{||}^2}{dt}$, following from kinetic energy conservation. In KIPP, the mirror force effect is implemented by way of shifting cells in the velocity space by very small distances (due to smallness of time steps) $\Delta v_{||}, \Delta v_{\perp}$ for each time step, with the subsequent sharing of the content of the shifted cell (constant f_e density inside the cell is assumed) among adjacent velocity grid cells $(v_{||}, v_{\perp})$.

Macroscopic effects of the above implementation of toroidal effects can be illustrated using the

parallel momentum balance equation from [25], which is consistent with the results of the rigorous analysis based on the transformation of the pressure stress tensor from Cartesian to field aligned coordinates [26l]. From Eq. (31) of [26], the parallel momentum balance equation of plasma species (electrons or ions), with the neglect of cross-field terms and external forces, reads:

$$\frac{\partial(nmV_{||})}{\partial t} = -\nabla_{||}(p_{||} + nmV_{||}^2) + (nmV_{||}^2 + p_{||} - p_{\perp})\nabla_{||}B/B + eZnE_{||} + R_{||}, \qquad (3)$$

where $p_{||}$ and $p_{\perp}$ are parallel and perpendicular (chaotic) pressures, $V_{||}$ - average parallel velocity, $eZnE_{||}$ and $R_{||}$ - electric field and friction forces. As one can see, compared to the situation with the spatially constant magnetic field, toroidicity leads to the appearance of the new term $(nmV_{||}^2 + p_{||} - p_{\perp})\nabla_{||}B/B$. Physically, as was demonstrated in [25], the $(nmV_{||}^2 + p_{||})\nabla_{||}B/B$ contribution to this extra term results from the expansion of the flux tube (different cross-sections at its two ends), while the $-p_{\perp}\nabla_{||}B/B$ contribution is attributed to the effect of the mirror force.

In KIPP, the variation of cell face areas and the effect of the mirror force can be switched on and off separately. In all KIPP cases presented in this paper toroidal geometry terms were switched on. Each of the two contributions to $(nmV_{||}^2 + p_{||} - p_{\perp})\nabla_{||}B/B$ in isolation were found to make an influence on KIPP results. Their effects however almost canceled each other out when both were switched on. For the momentum balance, this result could be expected, due to high degree of Maxwellization of thermal electrons (leading to $p_{e\perp} \approx p_{e||}$), negligible contribution of super-thermal electrons to electron pressure(s), and small $V_{||}$ relative to electron thermal velocity $v_{e,th}$. It was not entirely clear however why toroidal geometry terms didn't significantly influence electron parallel power fluxes and power deposition to divertor targets.

It has to be noted that toroidal effects are expected to influence ions much stronger than electrons. Extension of kinetic treatment onto ions is planned in the next version of KIPP.

7. Conclusions

Kinetic modelling with KIPP presented in this paper covers wide range of plasma conditions in the SOL and divertor regions, from attached plasmas (at divertor targets) with moderate T_e drops, to high recycling conditions with partial detachment and large T_e drops: from 90 eV upstream to below 1 eV at the targets. KIPP results are in a broad agreement with earlier studies on electron kinetic effects in SOL and divertor plasmas. In particular, they reveal electron heat (conductive power) flux limiting upstream (heat flux is lower than prescribed by Braginskii equations) and flux enhancement (heat flux is higher than according to Braginskii) downstream.

Deviations from Braginskii values in the main SOL, excluding the divertor, were found to be moderate, by factor ~ 1.5. Closer to, and at divertor targets, heat flux enhancement factors at slices (radial positions) with large T_e drops from upstream to the targets can be of order 10 or even higher. This is attributed to strong non-locality of electron power transport resulting in the appearance of extended tails or bump-on-tail features in the electron distribution functions. Such

large heat flux enhancement factors however occur under conditions where electron conductive power flux is low due to low T_e, so that electron convective power flux becomes comparable to, or even higher than the convective power flux. This indicates that, at least for the conditions modelled in this paper, kinetic effects of electron parallel transport are not expected to drastically change parallel profiles of plasma parameters in the SOL and divertor, including electron power fluxes at divertor targets. It is therefore likely that present day 2D fluid codes, such as EDGE2D or SOLPS, aren't too far off from reality in predicting divertor conditions, even when simple estimates based on mean free paths of super-thermal electrons point to the strong presence of kinetic effects rendering fluid equations incorrect.

It is important to stress however that a wider range of plasma conditions, e.g. in discharges with a much higher input power than analysed in this paper, including conditions expected in future fusion devices ITER and DEMO, may lead to different results of kinetic studies. Also, the inclusion of a kinetic model for ions, absent in the present work, may result in stronger kinetic effects, in particular for power fluxes to the target. Finally, the modelling described here is not a self-consistent kinetic modelling, since macroscopic plasma parameter profiles were taken from a fluid code EDGE2D. The use of kinetic ionization and excitation rates in a self-consistent kinetic modelling might produce profiles (e.g. profiles with steeper T_e gradients near the target) in which even electron kinetic transport effects (free-streaming) would be stronger than analysed in this work. The present results should therefore be considered as tentative, requiring confirmation under conditions with wider range of plasma parameters as well as extension of the kinetic treatment onto atomic rates.

Acknowledgement
This work has been carried out within the framework of the EUROfusion Consortium and has received funding from the Euratom research and training programme 2014-2018 under grant agreement No 633053. The views and opinions expressed herein do not necessarily reflect those of the European Commission. Discussions with Dr. D.P.Coster are acknowledged.

References

[1] Braginskii S I 1965 'Transport processes in a plasma', *Review of Plasma Physics* Vol. 1, edited by M.A.Leontovich (Consultants Bureau, New York) p.205
[2] Chodura R 1988 *Contrib. Plasma Phys.* **28** 303
[3] Fundamenski W 2015 *Plasma Phys. Control. Fusion* **47** R163
[4] Pitts R A et *al.* 2007 *Nucl. Fusion* **47** 1437
[5] Tskhakaya D *et al.* 2008 *Contrib. Plasma Phys.* **48** 89
[6] Tskhakaya D *et al.* 2009 *J Nucl. Mater.* **390-391** 335
[7] Stangeby P C 2000, The Boundary of Magnetic Fusion Devices, IOP Publishing, Bristol.
[8] Tskhakaya D 2017 *private communication*
[9] Batishchev O V *et al.* 1997 *Phys. Plasmas* **4** 1672
[10] Popova L *et al.* 2004 *Contrib. Plasma Phys*. **44** 252
[11] Allais F *et al.* 2005 *J. Nucl. Mater*. **337-339** 246
[12] Tskhakaya D 2016 *Contrib. Plasma Phys*. **56** 698
[13] Chankin A V, Coster D P, and Meisl G 2011 *Contrib. Plasma Phys*. **52** 500
[14] Chankn A V and Coster D P 2015 *J. Nucl. Mater*. **462** 498
[15] Simonini R *et al*. 1994 Contrib. *Plasma Phys*. **34** 368
[16] Reiter D 1992 *J. Nucl. Mater*. **196-198** 80
[17] Wiesen S *et al*. 2006 *ITC Project Rep*. http://www.eirene.de/e2deir_report_30jun06.pdf
[18] Trubnikov B A 1965, 'Particle interaction in a fully ionized plasma', *Review of Plasma Physics* Vol. 1, edited by M.A.Leontovich (Consultants Bureau, New York) p.105
[19] Kupfer K *et al.* 1996 *Phys. Plasmas* **3** 3544
[20] Zhao M, Chankin A V, and Coster D P 2017 *Nucl. Mater. and Energy* **12** 819
[21] Jaervinen A E *et al.* 2016 *Plasma Phys. Control. Fusion* **58** 045011
[22] Schneider R *et al.* 1992 *J. Nucl. Mater*. **196–198** 810
[23] Coster D *et al.* 2002 Proc. *19th IAEA Conf. on Fusion Energy* (Lyon, France, October 2002) CD-ROM paper IAEA-CN-94/TH/P2-13 (Vienna: IAEA)
[24] Huber A and Chankin A V 2017 *Plasma Phys. Control. Fusion* **59** 064007
[25] Zakharov L E and Shafranov V D 1986 'Equilibrium of current-carrying plasmas in toroidal configurations' *Reviews of Plasma Physics* Vol. 11, edited by M.A. Leontovich (Consultants Bureau, New York) p.153
[26] Chankin A V and Stangeby P C 2006 *Nucl. Fusion* **46** 975

Figures

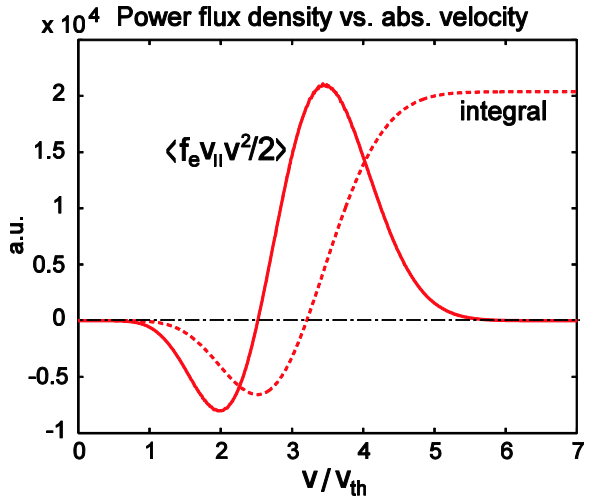

Fig. 1. Averaged electron power flux density and its integral vs. v/v_{th}, where v is total electron velocity and $v_{th} = \sqrt{T_e/m_e}$, from a KIPP case in a strongly collisional plasma. See text for details.

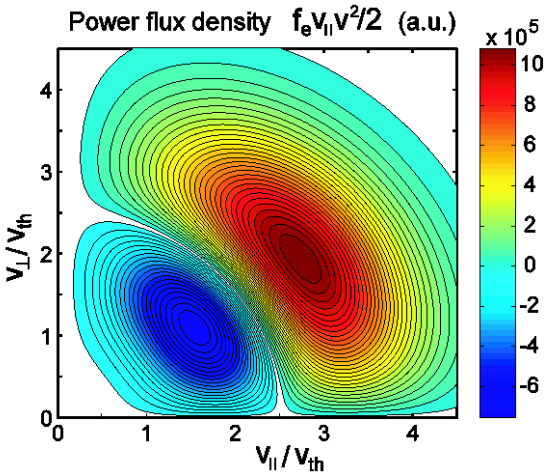

Fig. 2. 2D contour plot of the power flux density $f_e v_{||} v^2/2$ obtained in the same KIPP run for which results are shown in Fig. 1.

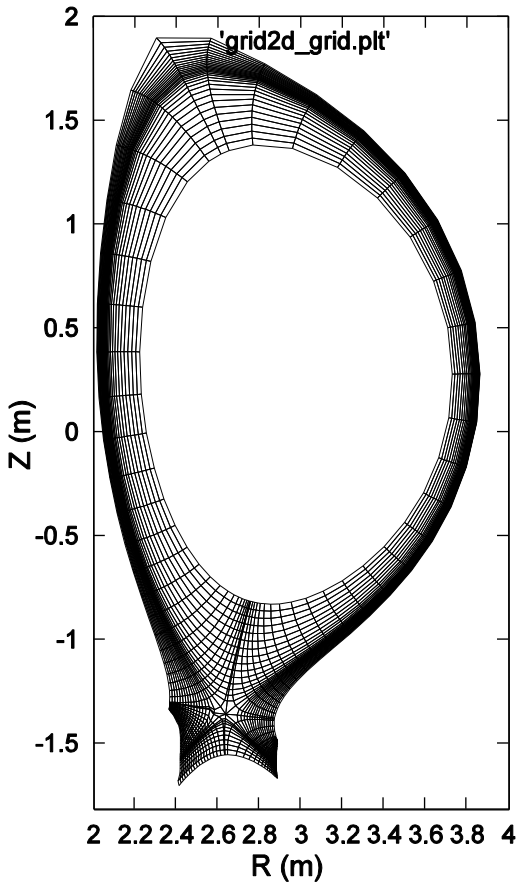

Fig. 3. EDGE2D grid used in the EDGE2D-EIRENE simulation.

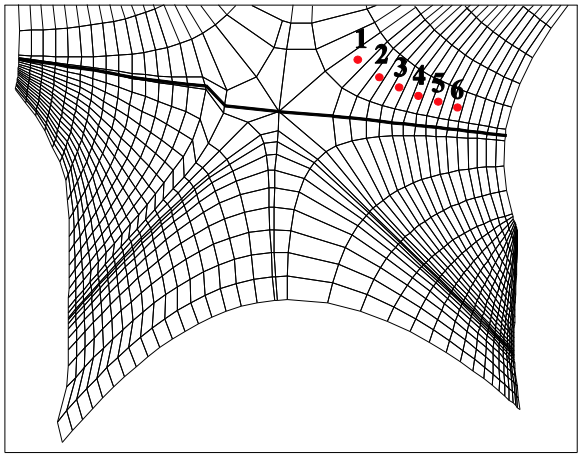

Fig. 4. Expanded view of the EDGE2D grid in the divertor region, showing numbered cells corresponding to radial positions of poloidal 'rings' (using EDGE2D nomenclature) which were chosen for KIPP runs. The chosen rings are referred to as 'slices' (for KIPP runs). Their numbering, given by index 'i' in the paper, doesn't coincide with the ring numbering in EDGE2D.

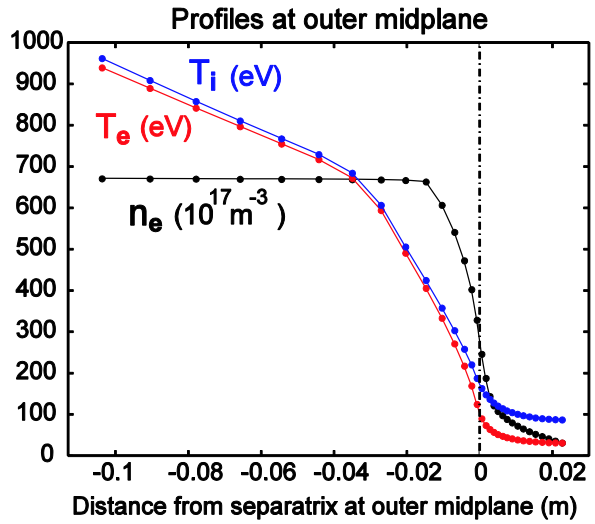

Fig. 5. Ion and electron temperatures and electron density profiles at the outer midplane position from the EDGE2D-EIRENE case vs. distance from the separatrix mapped to the plasma midplane.

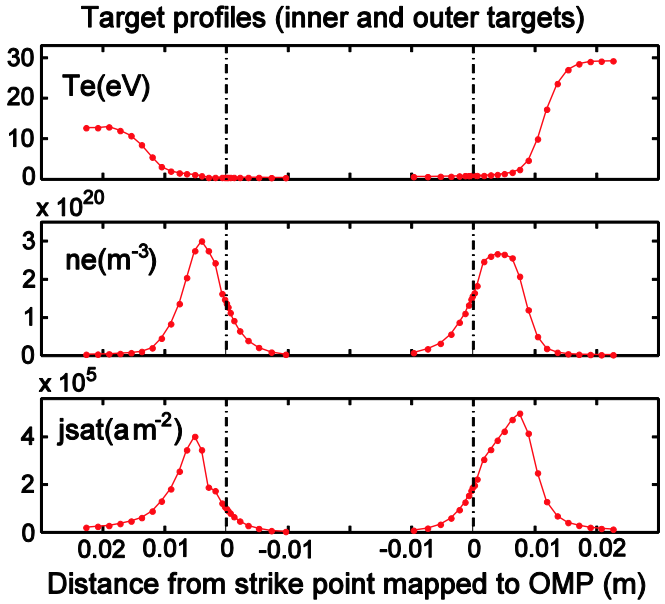

Fig. 6. Target profiles of T_e, n_e and ion saturation current density j_{sat} across target surfaces vs. distance from strike points mapped to the plasma midplane, for the selected EDGE2D-EIRENE case. Vertical dash-dotted lines indicate strike point (separatrix) positions. Positive distances refer to positions in the SOL, negative – to positions in the private flux region.

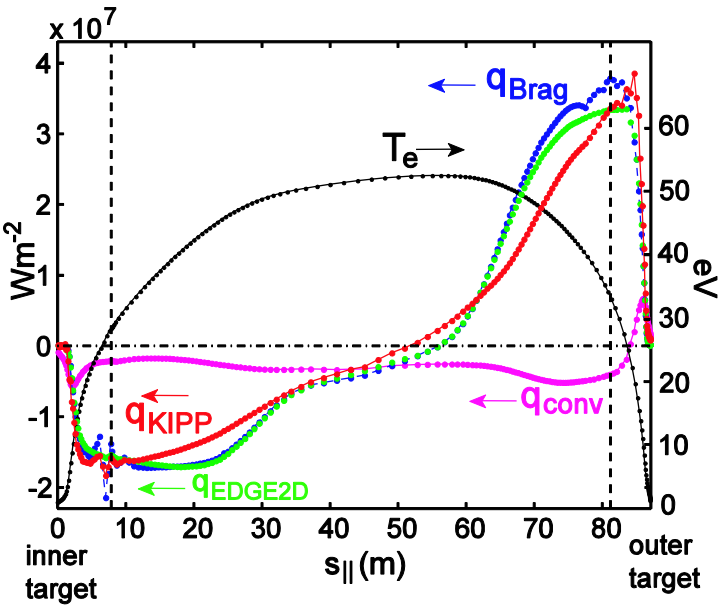

Fig. 7. Parallel profiles (along field lines) of electron conductive power fluxes q_{Brag}, q_{KIPP} and q_{EDGE2D}, together with profiles of electron convective power flux q_{conv} and electron temperature T_e, vs. distance along field lines, from the inner to outer target, for slice i = 3. Vertical dashed lines indicate positions of entrances to the divertor.

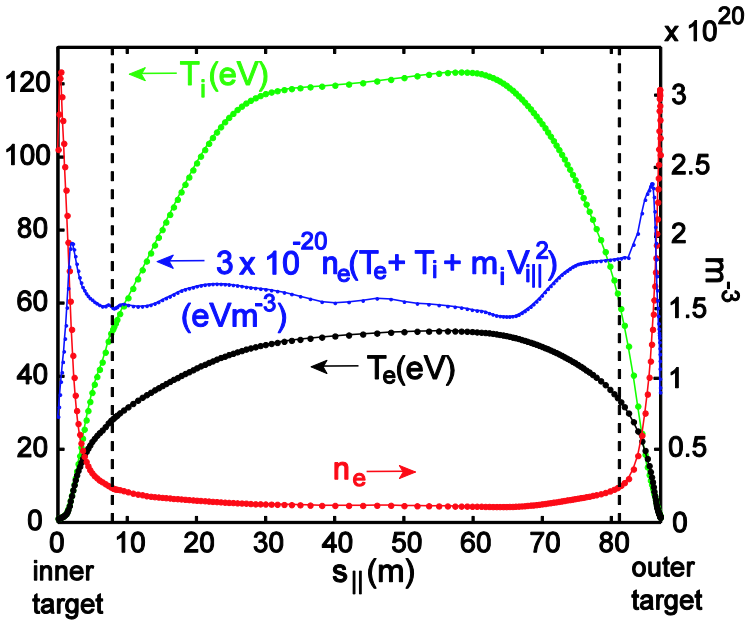

Fig. 8. Parallel profiles of electron and ion temperatures T_i and T_e, the quantity $n_e(T_e + T_i + m_i V_{i\|}^2)$ multiplied by 3×10^{-20}, and electron density n_e, vs. distance along field lines from the inner to outer target, for slice i = 3. Vertical dashed lines indicate positions of entrances to the divertor.

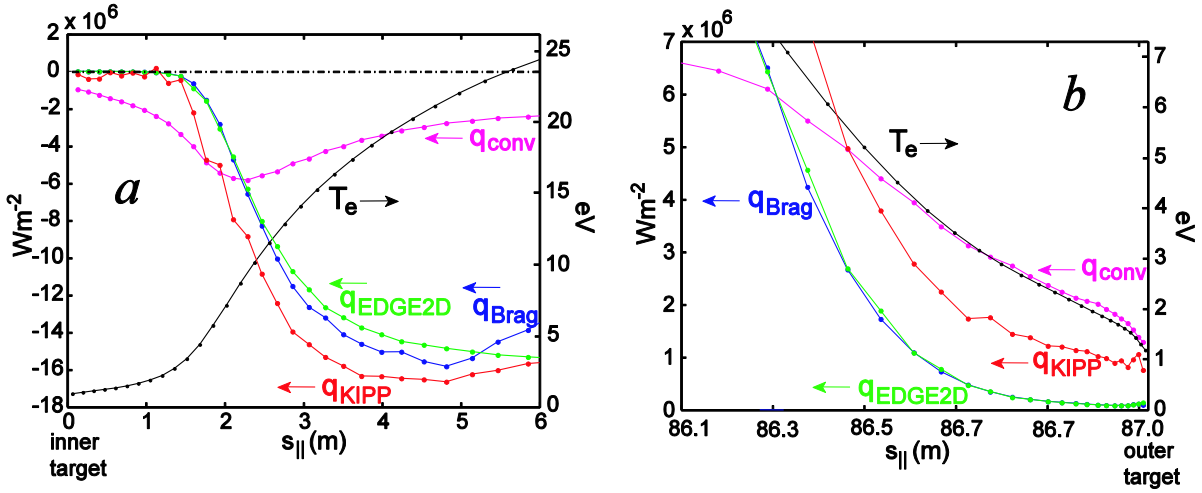

Figs. 9a,b. Same parameters as shown in Fig. 7 (for slice i = 3), but only in the inner (a) and outer (b) divertors.

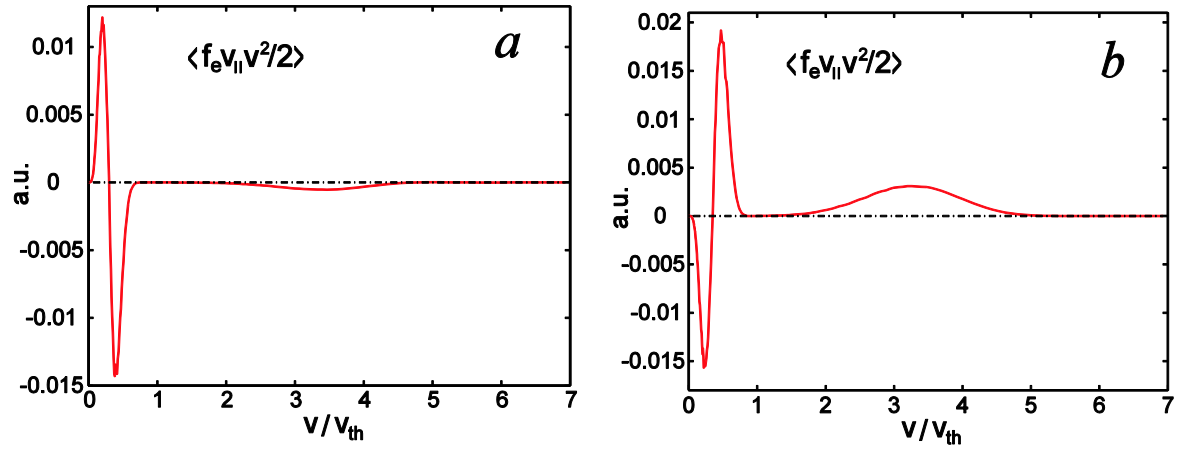

Figs. 10a,b. Conductive power flux density, including the velocity phase space factor, vs. dimensionless absolute velocity, for f_e at cells adjacent to the inner (a) and outer (b) targets, for slice i = 3. Thermal velocity v_{th} is calculated for the highest T_e upstream.

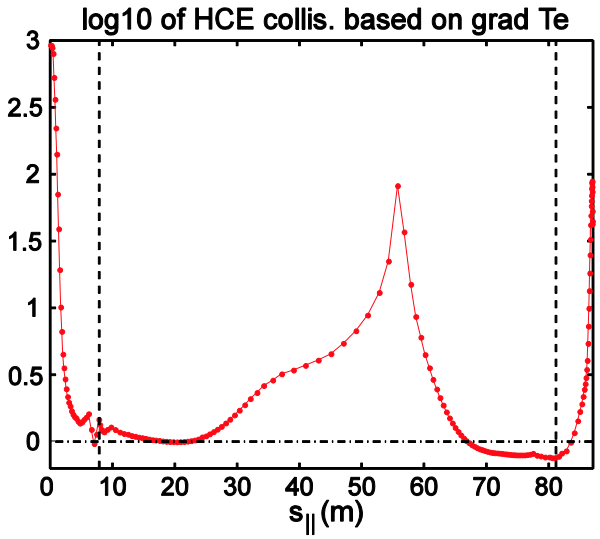

Fig. 11. log10 of dimensionless collisionality ν^*_{HCE}, calculated as electron dimensionless collisionality ν^* divided by 13, for slice i = 3. Vertical dashed lines indicate positions of entrances to the divertor.

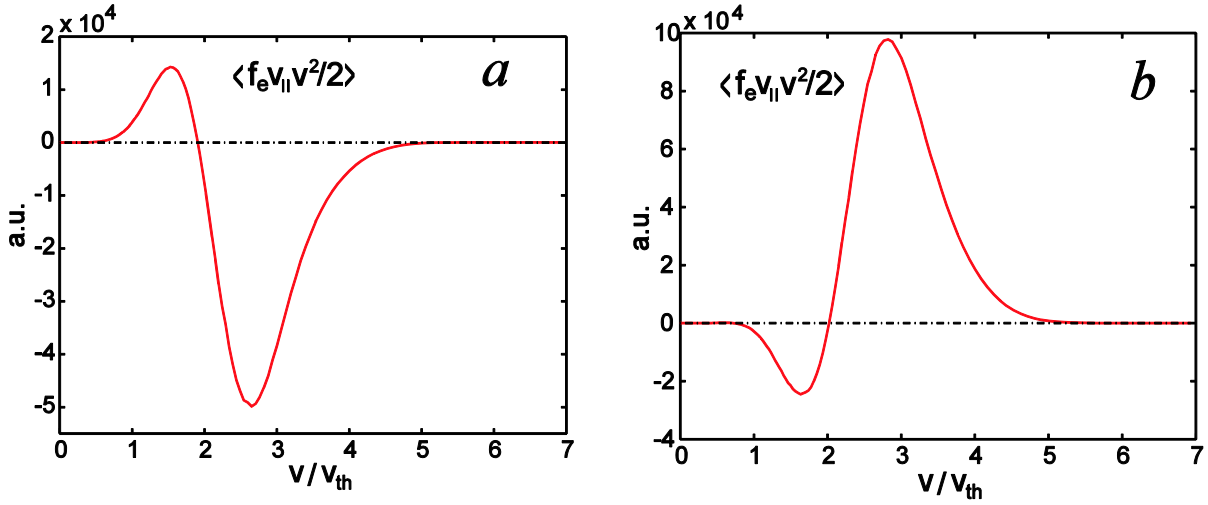

Figs. 12a,b. Conductive power flux density, including the velocity phase space factor, vs. dimensionless absolute velocity, for cells at the entrances to the inner (a) and outer (b) divertors, for slice i = 3. Thermal velocity v_{th} is calculated for the highest T_e upstream. Positions of entrances to divertors are indicated by vertical dashed lines in Fig. 7.

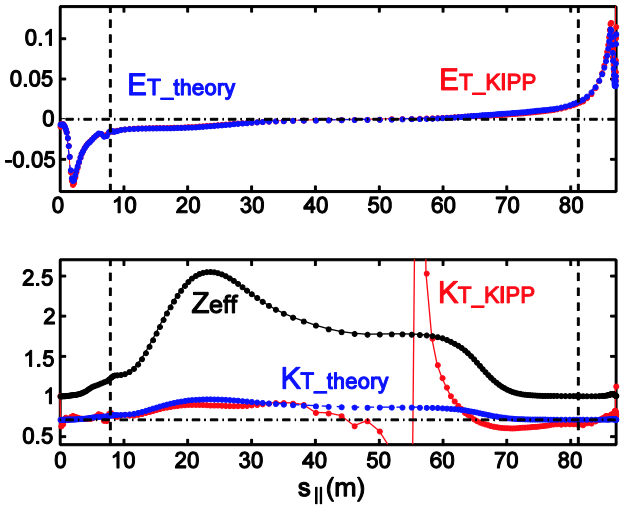

Fig. 13. Parallel profiles of the thermoforce electric field E_T, following from KIPP calculations and from the theoretical formula using the k_T coefficient (top box), and thermoforce coefficients k_T calculated using KIPP and the formula for $k_T(Z_{eff})$, together with the Z_{eff} profile (bottom box), for slice i = 3. The horizontal dash-dotted line in the bottom box corresponds to $k_T = 0.71$.

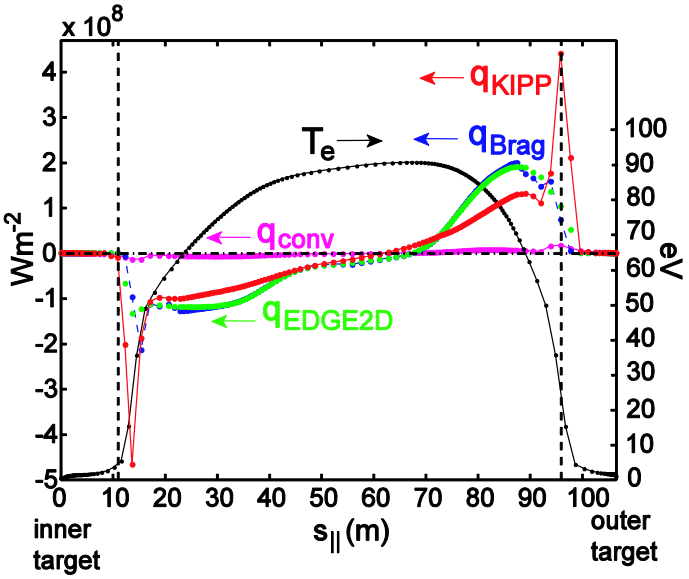

Fig. 14. Parallel profiles of electron conductive power fluxes q_{Brag}, q_{KIPP} and q_{EDGE2D}, together with profiles of electron convective power flux q_{conv} and electron temperature T_e, vs. distance along field lines, from the inner to outer target, for slice i = 1. Vertical dashed lines indicate positions of entrances to the divertor.

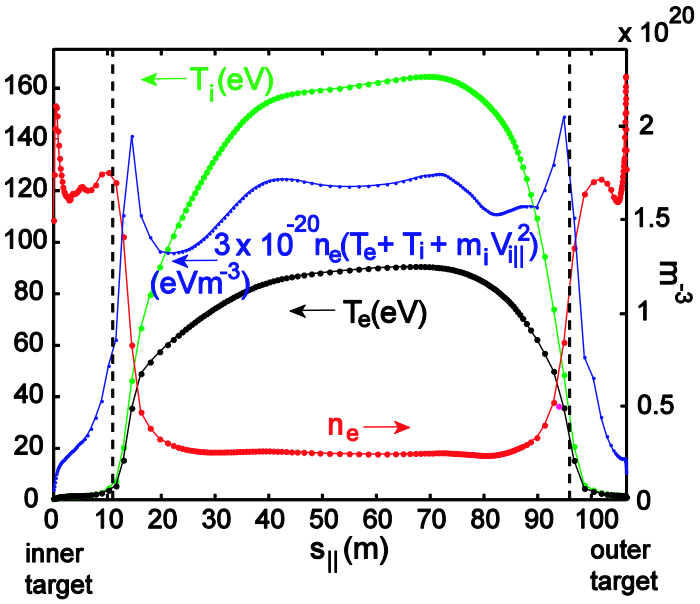

Fig. 15. Parallel profiles of electron and ion temperatures T_i and T_e, the quantity $n_e(T_e + T_i + m_i V_{i\|}^2)$ multiplied by 3×10^{-20}, and electron density n_e, vs. distance along field lines from the inner to outer target, for slice i = 1. Vertical dashed lines indicate positions of entrances to the divertor.

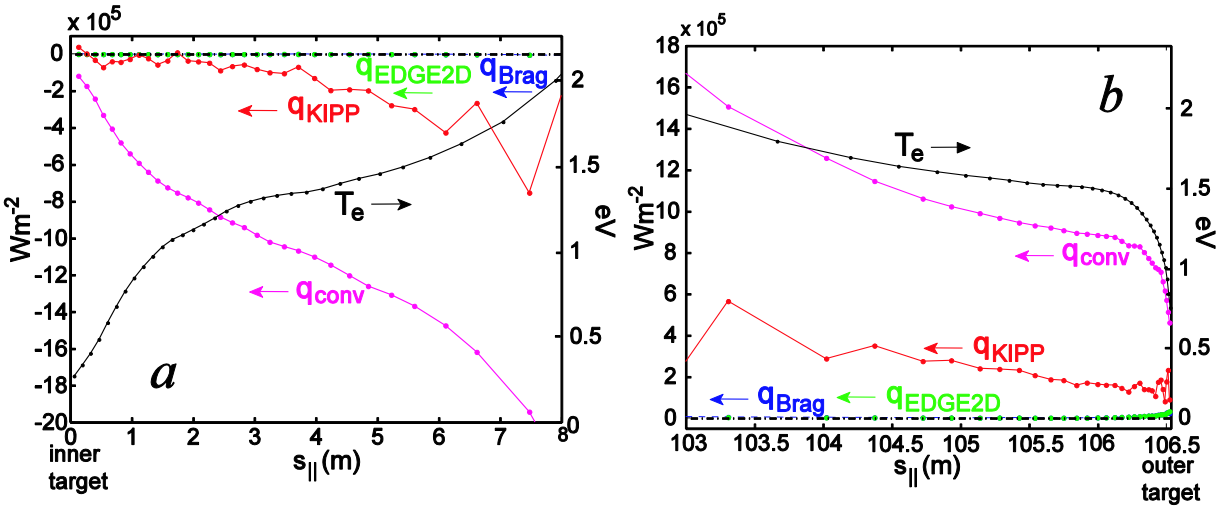

Figs. 16a,b. Same parameters as shown in Fig. 14 (for slice i = 1), but only in the inner (a) and outer (b) divertors.

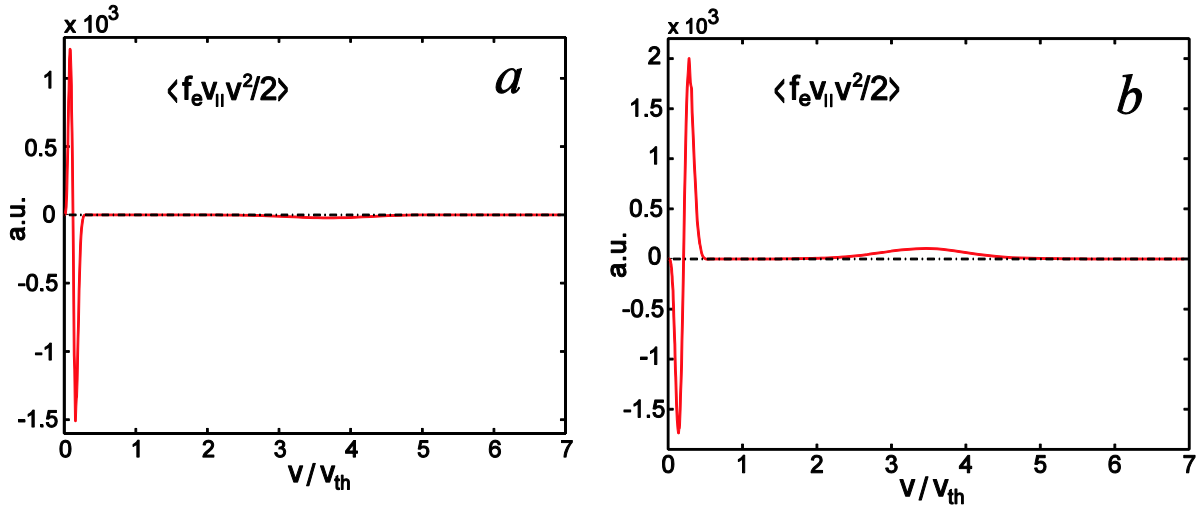

Figs. 17a,b. Conductive power flux density, including the velocity phase space factor, vs. dimensionless absolute velocity, for f_e at cells adjacent to the inner (a) and outer (b) targets, for slice i = 1. Thermal velocity v_{th} is calculated for the highest T_e upstream.

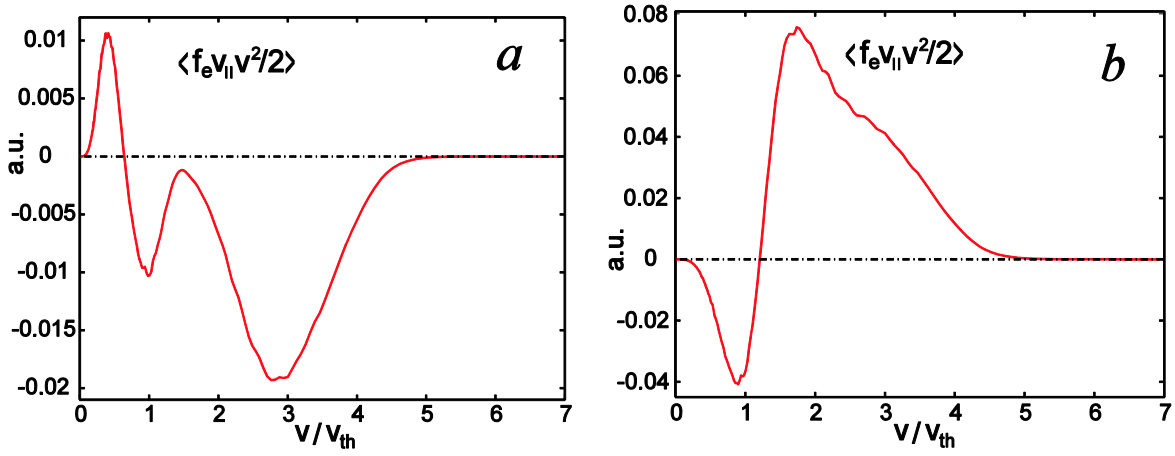

Figs. 18a,b. Conductive power flux density, including the velocity phase space factor, vs. dimensionless absolute velocity, for cells at the entrances to the inner (a) and outer (b) divertors, for slice i = 1. Thermal velocity v_{th} is calculated for the highest T_e upstream. Positions of entrances to divertors are indicated by vertical dashed lines in Fig. 14.

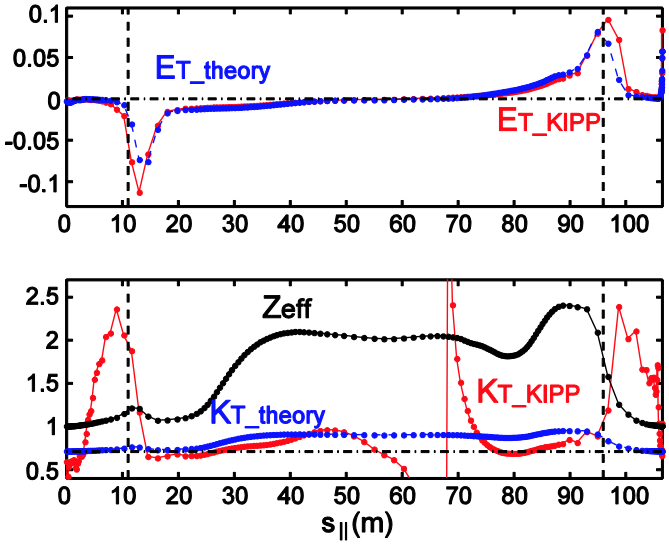

Fig. 19. Parallel profiles of the thermoforce electric field E_T, following from KIPP calculations and from the theoretical formula using the k_T coefficient (top box), and thermoforce coefficients k_T calculated using KIPP and the formula for $k_T(Z_{eff})$, together with the Z_{eff} profile (bottom box), for slice i = 1. The horizontal dash-dotted line in the bottom box corresponds to $k_T = 0.71$.

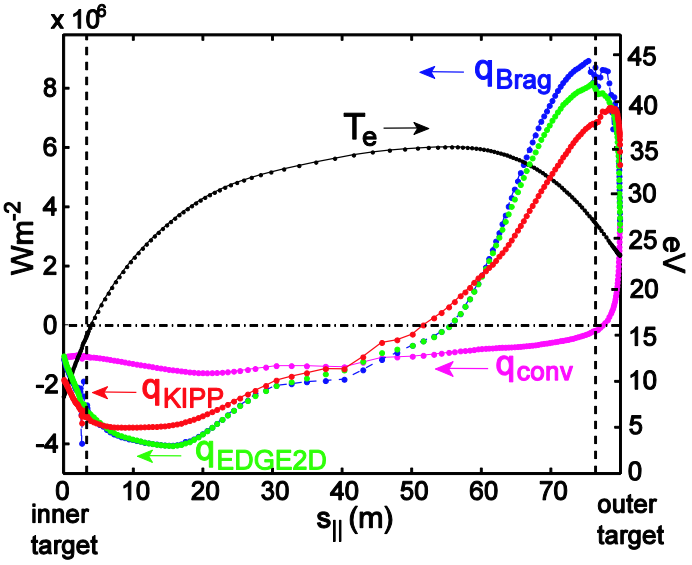

Fig. 20. Parallel profiles of electron conductive power fluxes q_{Brag}, q_{KIPP} and q_{EDGE2D}, together with profiles of electron convective power flux q_{conv} and electron temperature T_e, vs. distance along field lines, from the inner to outer target, for slice i = 6. Vertical dashed lines indicate positions of entrances to the divertor.

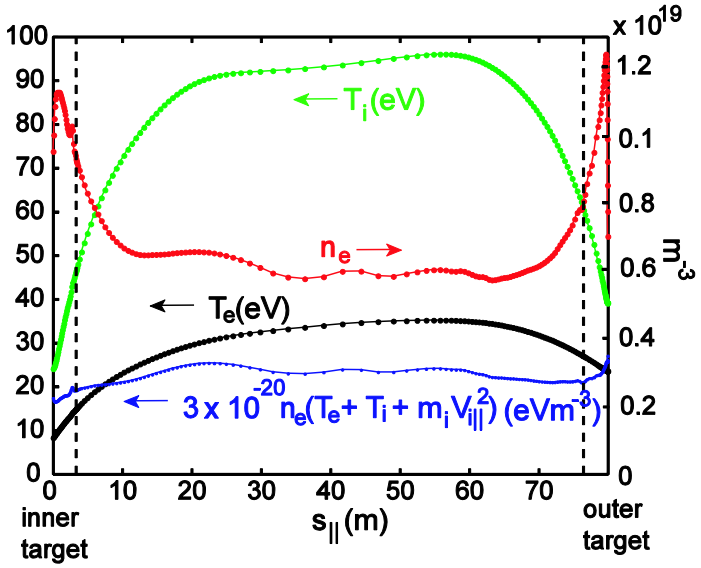

Fig. 21. Parallel profiles of electron and ion temperatures T_i and T_e, the quantity $n_e(T_e + T_i + m_i V_{i\|}^2)$ multiplied by 3×10^{-20}, and electron density n_e, vs. distance along field lines from the inner to outer target, for slice i = 6. Vertical dashed lines indicate positions of entrances to the divertor.

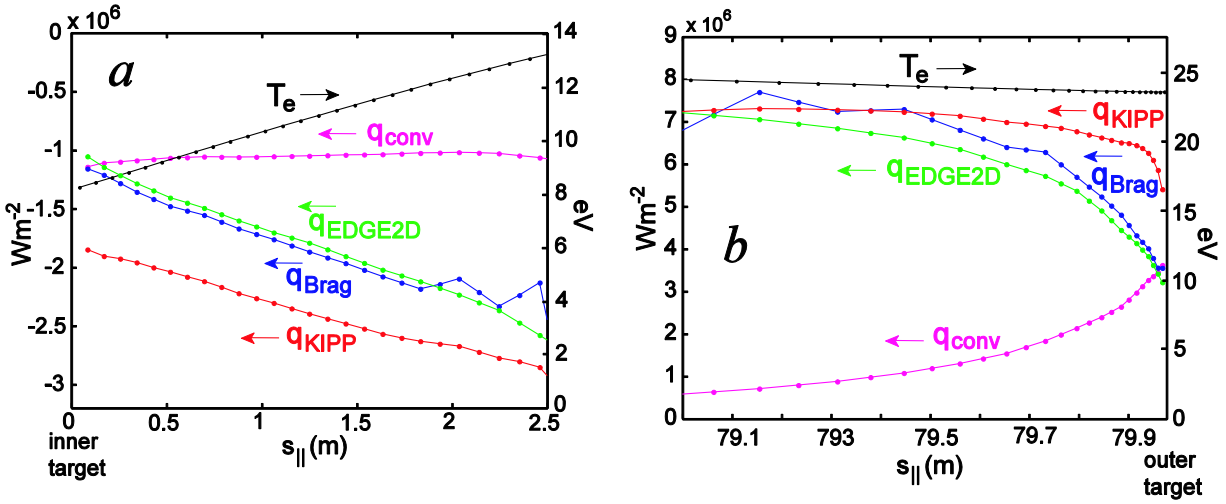

Figs. 22a,b. Same parameters as shown in Fig. 20 (for slice i = 6), but only in the inner (a) and outer (b) divertors.

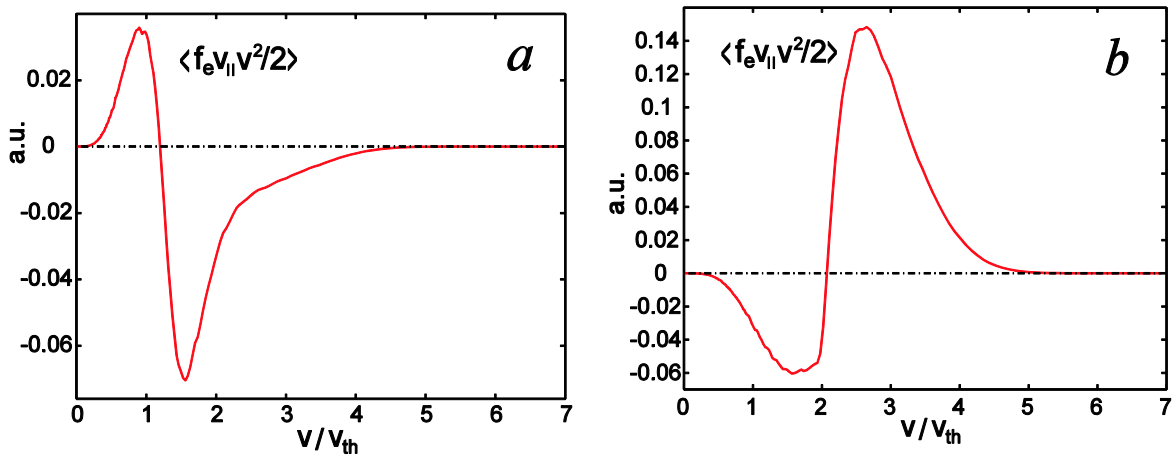

Figs. 23a,b. Conductive power flux density, including the velocity phase space factor, vs. dimensionless absolute velocity, for f_e at cells adjacent to the inner (a) and outer (b) targets, for slice i = 6. Thermal velocity v_{th} is calculated for the highest T_e upstream.

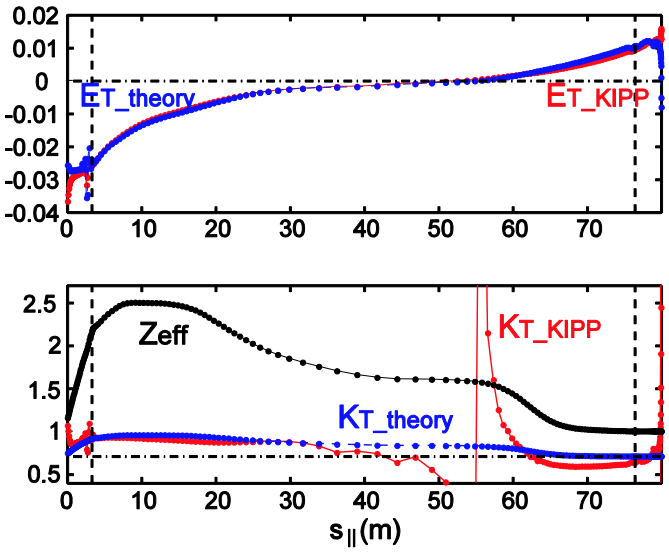

Fig. 24. Parallel profiles of the thermoforce electric field E_T, following from KIPP calculations and from the theoretical formula using the k_T coefficient (top box), and thermoforce coefficients k_T calculated using KIPP and the formula for $k_T(Z_{eff})$, together with the Z_{eff} profile (bottom box), for slice i = 6. The horizontal dash-dotted line in the bottom box corresponds to $k_T = 0.71$.

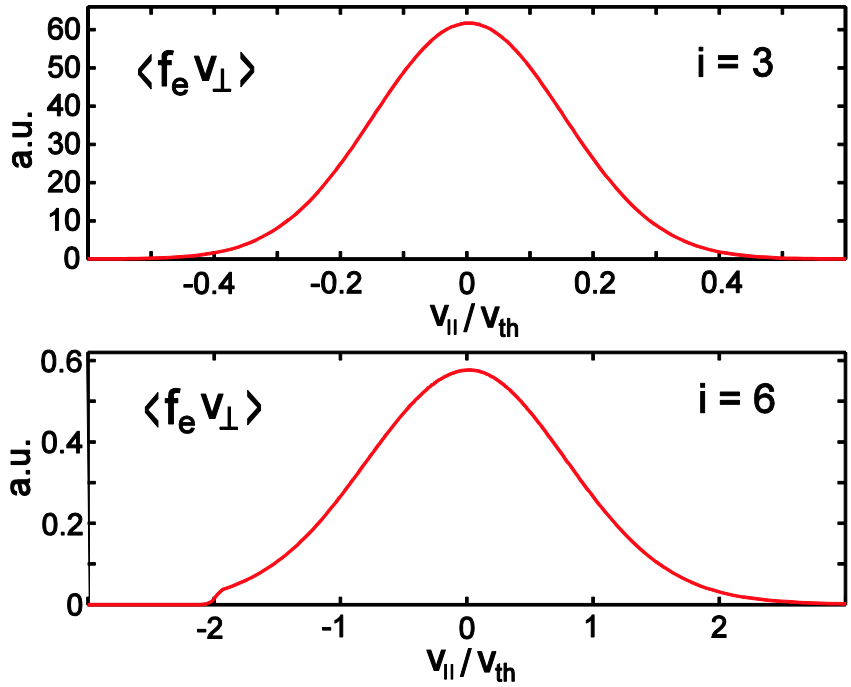

Fig. 25. Averaged over perpendicular velocity electron distribution functions f_e at boundary cells adjacent to outer targets for slices i = 6 and 3. Axes values are not related to each other, since velocities were normalized using highest upstream T_e for each slice separately. For i = 6, the Debye sheath cut-off effect can be seen at $v_{||} / v_{\perp} \approx -2$.